Graphene–Nanotube–Iron Hierarchical Nanostructure as Lithium Ion Battery Anode
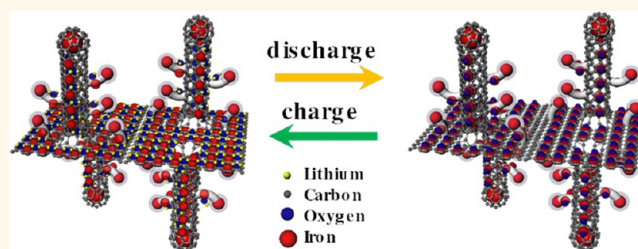
Si-Hwa Lee,[†] Vadahanambi Sridhar,[†] Jung-Hwan Jung,[†,‡] Kaliyappan Karthikeyan,[§] Yun-Sung Lee,[§] Rahul Mukherjee,[⊥] Nikhil Koratkar,[⊥] and Il-Kwon Oh[†,*]

[†]Graphene Research Center, KAIST Institute of NanoCentury, School of Mechanical, Aerospace and Systems Engineering, Division of Ocean Systems Engineering, Korea Advanced Institute of Science and Technology (KAIST), 291 Daehak-ro, Yuseong-gu, Daejeon 305-701, Republic of Korea, [‡]A. G. MacDiarmid NanoTech Institute, University of Texas at Dallas, Richardson, Texas 75080, United States, [§]Faculty of Applied Chemical Engineering, Chonnam National University, 77 Yongbong-ro, Buk-gu, Gwangju 500-757, Republic of Korea, and [⊥]Department of Mechanical, Aerospace and Nuclear Engineering, Rensselaer Polytechnic Institute, 4009 Jonsson Engineering Center, Troy, New York 12180, United States

ABSTRACT In this study, we report a novel route *via* microwave irradiation to synthesize a bio-inspired hierarchical graphene–nanotube–iron three-dimensional nanostructure as an anode material in lithium-ion batteries. The nanostructure comprises vertically aligned carbon nanotubes grown directly on graphene sheets along with shorter branches of carbon nanotubes stemming out from both the graphene sheets and the vertically aligned carbon nanotubes. This bio-inspired hierarchical structure provides a three-dimensional conductive network for efficient charge-transfer and prevents the agglomeration and restacking of the graphene sheets enabling Li-ions to have greater access to the electrode material. In addition, functional iron-oxide nanoparticles decorated within the three-dimensional hierarchical structure provides outstanding lithium storage characteristics, resulting in very high specific capacities. The anode material delivers a reversible capacity of ~1024 mA·h·g^{-1} even after prolonged cycling along with a Coulombic efficiency in excess of 99%, which reflects the ability of the hierarchical network to prevent agglomeration of the iron-oxide nanoparticles.

KEYWORDS: bio-inspired hierarchy · graphene-nanotube–iron composite · three-dimensional nanostructure · anode material · lithium-ion batteries

The recent discovery of graphene, a free-standing two-dimensional (2D) carbon material,[1,2] has garnered global attention due to its outstanding mechanical,[3] thermal,[4] and electrical[5] properties. Graphene has been exploited in a wide range of applications, including supercapacitors,[6] batteries,[7] solar cells,[8] actuators,[9] sensors,[10] composites,[11] and hydrogels.[12] Also, graphene has been used as a substrate to make metal-decorated graphenes with various applications, such as sensors,[13] catalyst supports,[14] anode materials for lithium ion batteries[15] and so on. Functionalized graphene nanohybrid and three-dimensional nanostructure based on graphene as the substrate have recently attracted attention due to their high surface-to-volume ratio, electrochemical characteristics, and reduced agglomeration originating from their unique structural morphology and spacer role.

Such graphene nanohybrids have proven to be advantageous in applications such as water treatment,[16] superhydrophobic surfaces,[17] transparent conductive films,[18] mechanically compliant films,[19] electrodes for secondary batteries and solar cells.[20]

Though there have been some reports on the integration of one-dimensional (1D) metal nanorods and nanospikes on 2D graphene sheets to produce heterogeneous three-dimensional (3D) arrays,[21] the overall specific surface area of such architectures is relatively low since the metal nanorods are solid structure. One way to overcome this drawback is to grow 1D carbon nanotubes on graphene and to decorate zero-dimensional (0D) metal nanoparticles on their surfaces. If metal oxide nanoparticles, such as MnO_2, TiO_2, Fe_2O_3, Co_3O_4 and NiO, can be decorated on the 3D carbon

nanostructure, the resulting hybrid structures may offer exciting possibilities to improve the performance of Li-ion batteries among other applications.[22] While we have previously shown the feasibility of growing nanotube stems off graphene surfaces,[23] the combination of 0D, 1D and 2D nanomaterials in one single system with larger primary nanotube stems and smaller secondary nanotube branches growing off these stems has not been synthesized until now. It should be noted that such structural hierarchy[24] is commonly observed in most biological systems including chromosomes, proteins, cells, tissues, and organisms. Natural biomaterials, such as shell,[25] bone,[26] tendons[27] and the attachment pads of geckos[28] consist of multiscale and multilevel self-similar hierarchical structures. There are many advantages of such a structure in terms of arresting crack propagation, high mechanical stiffness and toughness, ultrahigh surface-to-volume ratio, improved biochemical activities, and efficient fluidic channel transport. Many groups have synthesized hierarchically structured materials to improve the performance of functional materials used in applications, such as optoelectronics,[29] biomedicine,[30] and energy storage.[31] However, it still remains an enormous challenge to synthesize a hierarchical 3D nanostructure that integrates 0D, 1D and 2D materials in a single network.

Here, we report a novel microwave-assisted synthesis method for the production of a hierarchical 3D nanostructure as an anode material in lithium ion batteries, based on a combination of graphene, carbon nanotube, and iron nanoparticles. The 3D graphene—nanotube—iron (G-CNT-Fe) nanostructure is composd of stem carbon nanotubes grown on graphene sheets and much smaller branched carbon nanotubes which are grown again on both the stem nanotubes and on the graphenes. In addition, functional 0D iron nanoparticles are attached both on 1D nanotubes and 2D graphene sheets. This microwave irradiation method is very attractive for large-scale synthesis of such unique 3D nanostructure. The synthesized hierarchical 3D nanomaterial shows significant potential as an ultrahigh capacity anode material in lithium ion batteries.

RESULTS AND DISCUSSION

Synthesis and Mechanism. The entire scheme of synthesis and the growth mechanism are depicted schematically in Figure 1. Organometallic chemical compounds, such as ferrocene, can be decomposed into both a hydrocarbon supplier and a metal catalyst precursor under microwave irradiation. To obtain the hierarchical G-CNT-Fe 3D nanostructure, a novel and
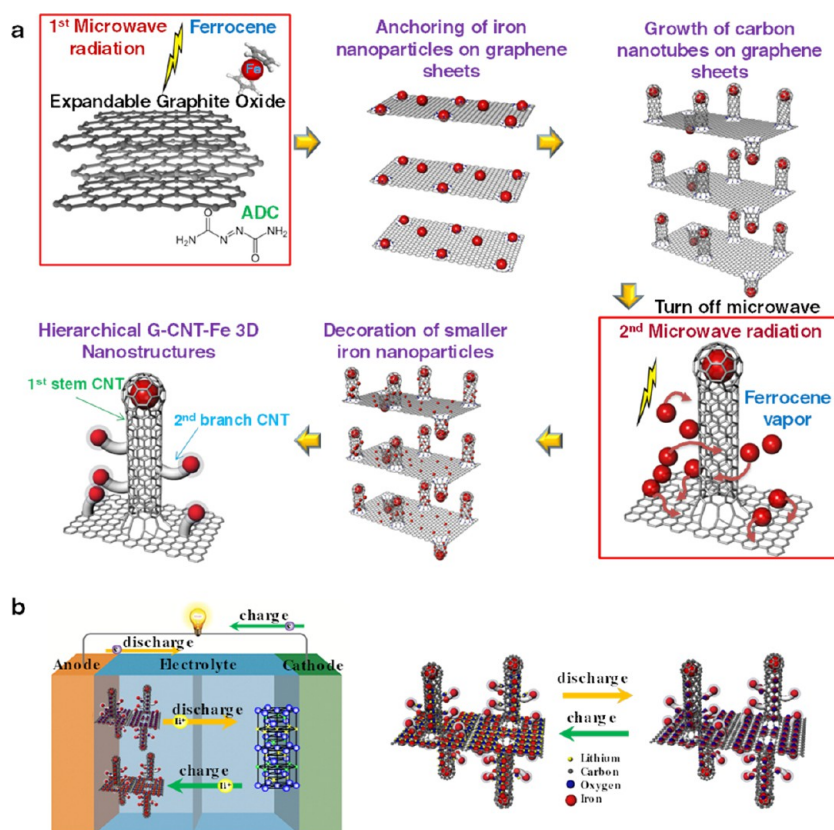

Figure 1. Two-step synthesis of hierarchical G-CNT-Fe 3D nanostructure and its application to anode material in lithium ion batteries. (a) Step 1, microwave reaction for carbon nanotube growth, and Step 2, iron nanoparticle decoration and fast explosive growth of smaller carbon nanotubes on original carbon nanotubes and graphene. (b) Schematic diagram for charge and discharge in G-CNT-Fe 3D anode material.

simple two-step process was developed by exposing the mixture of ferrocene, azodicarbonamide (ADC) and expandable graphite oxide platelets to multiple microwave irradiation cycles.

Under microwave irradiation, three different phenomena occur simultaneously during the synthesis of G-CNT-Fe nanohybrids. The first is microwave-induced expansion of few-layered graphene oxide to graphene nanoworms. This expansion is further augmented by the presence of gaseous products from the decomposition of azodicarbonamide (ADC), which releases large amounts of CO_2 and N_2, resulting in further expansion along the c-axis of the graphene worms. A byproduct of ADC decomposition is urea, which reacts with oxygen moieties, such as carboxyl, hydroxyl, and carbonyl groups of the graphene oxide surface to graft amine groups. The initial anchoring of iron nanoparticles on graphene sheets in the first step is shown in Figure 1a. Next, stem carbon nanotubes are grown through the first microwave irradiation. The formation of carbon nanotubes is initiated from the decomposition of ferrocene vapor under microwave irradiation, resulting in generation of catalyst particles and release of hydrocarbon fragments. The iron catalyst particles formed by collision processes are anchored on graphene surfaces and induce the growth of carbon nanotubes. When the microwave radiation is turned off, the cooled ferrocene vapor attaches to the 3D nanostructure, and much smaller carbon nanotubes are grown on the 3D nanostructure under the second microwave irradiation, resulting in the formation of hierarchical G-CNT-Fe 3D nanostructure as show in Figure 1a.

In this study, to investigate the potential application of the hierarchical G-CNT-Fe nanostructure as an anode material for lithium ion batteries, galvanostatic charge−discharge studies were carried out as depicted schematically in Figure 1b. In a conventional Li-ion battery, the cathode materials are typically inorganic compounds, such as transition metal oxides, characterized by layered or tunneled structures. The extracted lithium ions from lithium metal oxide cathodes are inserted into a graphitic carbon anode during the charge process. In the discharge cycle, lithium ions inserted into the carbon layers can be readily extracted and transported back to the cathode. Figure 1b shows that the ideal crystal structure of layered $LiMO_2$ (M = Co, Ni) has a close-packed oxygen array which is slightly distorted from ideal cubic close packing. Transition metal ions such as nickel and cobalt ions are surrounded by six oxygen atoms forming MO_2 infinite slabs by edge-sharing of the MO_6 octahedra. Lithium ions are located between the MO_2 layers in octahedral sites. In our system, we expect that during the charging process, the reduction of Fe^{3+} ions to metallic Fe^0 and the formation of amorphous Li_2O will occur. Large amounts of Li ions can therefore be stored and

released in the Fe_2O_3 structure through the formation and decomposition of Li_2O respectively, accompanied by the redox reaction of metallic iron during the anodic process.

Morphology of 3D Carbon Nanostructure. To characterize the morphology changes of the carbon nanostructure during the synthesis process, SEM micrographs of the hierarchical G-CNT-Fe 3D nanostructure are provided in Figure 2. The structure of as-prepared graphene oxide layers is shown in Figure 2a. The defect sites of graphene oxide act as good anchoring points for ferrocene. With further increase in the time of microwave irradiation, the ferrocene sublimes to yield G-CNT-Fe hybrids. Figure 2b,c shows that CNTs with very high density are grown on graphene sheets and are distributed uniformly across the graphene worms. Figure 2d shows that iron nanoparticles are attached on both the graphene surfaces and carbon nanotubes, but the density is slightly higher at the edges of the graphene sheets. This observation can be attributed to the predominant distribution of amine groups at the edges of the graphene sheets. The black tips in Figure 2b indicate that iron nanoparticles induce the growth of carbon nanotubes, a phenomenon termed as "tip growth mechanism". The ultra-high resolution SEM micrograph shown in Figure 2c indicates that the carbon nanotubes are firmly anchored on the graphene surface, which in turn confirms that the nanotubes grow `from' the graphene substrate, rather than in the vapor phase as in CVD synthesis. Furthermore, Figure 2d shows the presence of some iron nanoparticle aggregates along the nanotube surface and on the graphene surface. After the second microwave irradiation, Figure 2e shows the growth of shorter branches of carbon nanotubes on the stem carbon nanotubes, resulting in hierarchical G-CNT-Fe 3D nanostructure. Consequently, microscale hierarchical G-CNT-Fe 3D structure can be readily produced through our simple two-step microwave synthesis technique as shown in Figure 2f.

SEM and TEM images of hierarchical G-CNT-Fe nanostructure are shown in Figure 3. It can be clearly seen that the carbon nanotubes are standing vertically on a graphene sheet, and some iron nanoparticles are decorated on both the carbon nanotubes and the graphene surface as shown in Figure 3a. The HRTEM image of an individual nanotube shows that a large iron nanoparticle is encapsulated and located at the tip of the carbon nanotube. The carbon nanotube is microscale in length and has a bamboo-like structure with iron nanoparticles adhering to the sidewalls as shown in Figure 3b. On the basis of the shape of compartments or "knots", the bamboo carbon nanotubes (BCNTs) can be divided into two broad categories, namely, complete and incomplete knots.[32] The HRTEM images of the BCNTs reveal the formation of complete knots, wherein the inner graphene
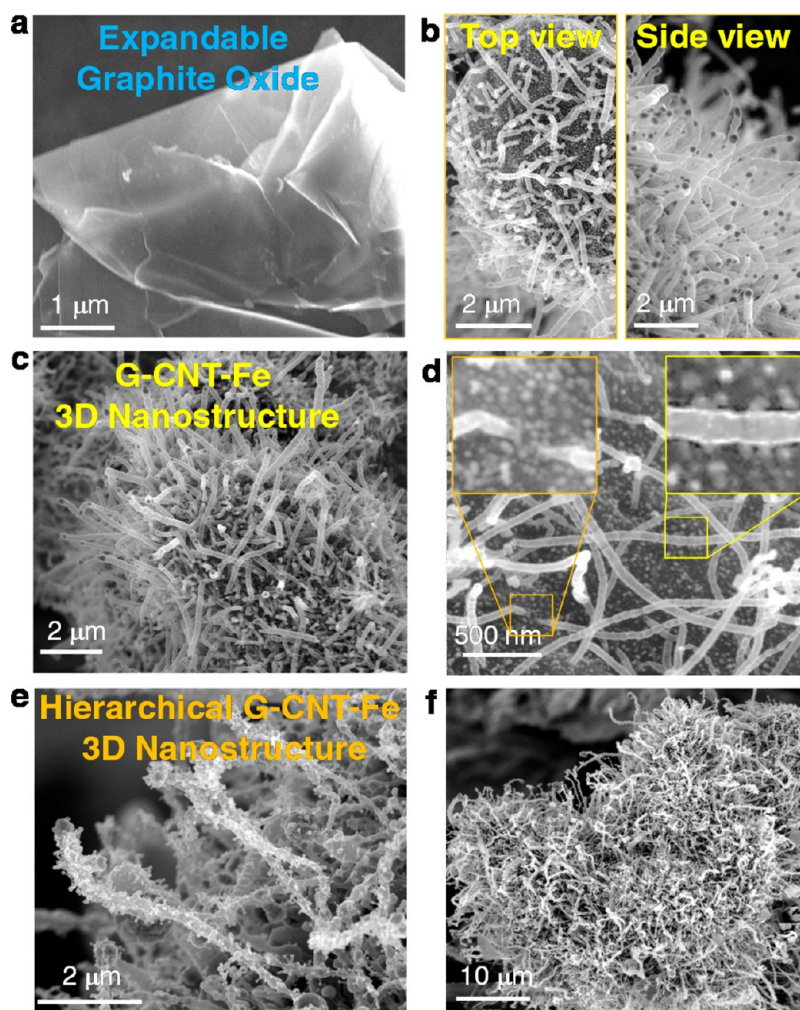
Figure 2. SEM images demonstrating step-by-step synthesis of hierarchical G-CNT-Fe 3D nanostructure. (a) Expandable few-layered graphene platelet, (b) initial growth of carbon nanotubes on graphene sheet in the first step, (c) fully grown G-CNT-Fe 3D nanostructure through the first microwave radiation, (d) initial attachment of iron nanoparticles in the second step, (e) growth of smaller branched carbon nanotubes on the first stem carbon nanotubes grown in the second step microwave radiation, and (f) microscale hierarchical G-CNT-Fe 3D nanostructure.

compartment layers are fully formed, elongated, and have completely bridged the inner diameter of the outer tube. The diameter of each knot is in the rage of 100−120 nm, and the length of the knots is about 200−250 nm. HRTEM images also exhibit the presence of iron nanoparticulates adhering to the outer edges of the nanotubes, displaying morphology of iron-decorated BCNTs anchored onto the graphene surface. The iron particles are well distributed along the side-wall of the bamboo CNTs with occasional clustering and agglomeration. Low- and high-resolution dark-field HADF images in Figure 3c show the multilevel spatial distribution of iron particles with some aggregation.

The inset in Figure 3c shows an iron EDX scan. Since iron nanoparticles are catalytically active, they intro-duce additional functionality to the G-CNT-Fe nano-hybrid and open up new potential applications, such as anode materials for lithium ion batteries. Figure 3d shows hierarchical G-CNT-Fe 3D nanostructure which

was synthesized with the two-step microwave irradia-tion method. The stem CNTs were formed with a diam-eter ranging from 40 to 60 nm. The second branched CNTs grow on the stem CNTs and have a diameter between 10 to 20 nm.

Such a reduction in diameter from the stem CNT to the branched CNT mimics the structural hierarchy that is commonly observed in biological systems. Each stem and branched CNT has an iron nanoparticle at its tip, thus inducing the growth of CNTs. The second branched CNT was formed from the stem CNT through the tip growth mechanism as shown in Figure 3e. While a big flower-like iron nanoparticle at the tip of the first stem CNT can be observed in Figure 3d, a smaller iron nanoparticle is encapsulated at the tip of the second branch CNT, as shown in Figure 3e. The nanostructure of G-CNT-Fe was further evaluated with *in situ* TEM. Much smaller iron nanoparticles with a diameter of 5−8 nm are observed on the surface of the second branched CNTs, as con-firmed by the TEM image included in Figure 3**f**.
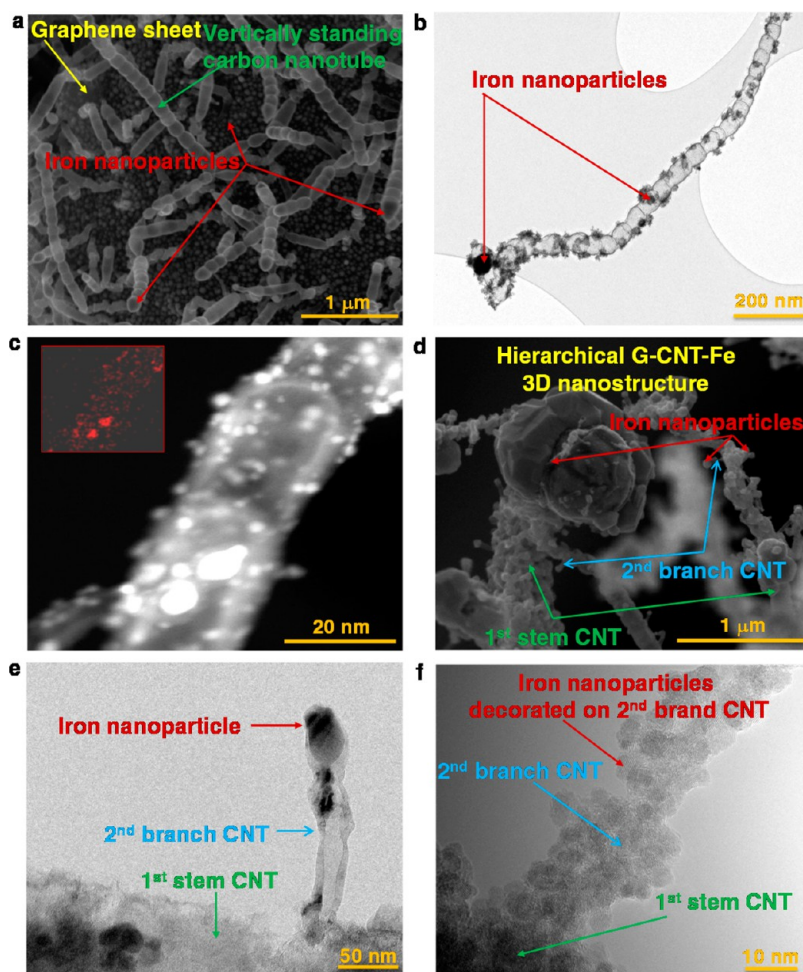
Figure 3. SEM image of hierarchical graphene−nanotube−iron 3D nanostructure. (a) Vertically standing carbon nanotubes on graphene sheets; (b) HRTEM of individual nanotube showing bamboo structure of nanotubes with iron nanoparticles adhering to the sidewalls; (c) low-and high-resolution dark-field HADF images showing the multilevel distribution of iron particles with some extent of aggregation at lower resolution and at high resolution, the inset shows an iron EDX scan; (d) hierarchical G-CNT-Fe 3D nanostructure showing first stem and branch CNTs; (e) second branch CNTs grown on the first stem CNTs; (f) iron nanoparticles decorated on the second branch CNTs.

Chemical Structure Analysis. The chemical structure of these iron particles was evaluated by XPS analysis, and the results are shown in Figure 4. The XPS Fe2p spectrum in Figure 4a shows two peaks at 711.5 and 724.7 eV, which are assigned to the $Fe2p_{3/2}$ and $Fe2p_{1/2}$ binding energies, respectively. The chemical nature of these moieties can be obtained from the deconvoluted O1s XPS spectra plotted in Figure 4b, which show three peaks at 530.1, 531.6, and 533 eV, indicating the presence of O^2, OH^-, and H_2O, respectively. These results indicate that the iron particles exist in a mixed state of Fe_2O_3 and FeOOH. To further validate the existence of multiple valences of iron particles, we obtained EELS spectra of iron particles as plotted in Figure 4c. The EELS analysis of the Fe $L_{2,3}$ provides information on the variation of the valence state of iron phase. The iron particles inside the CNTs show a sharp L_3 peak and a smaller L_2 peak at a distance of 12.6 eV, indicating zero valence iron, whereas the iron outside the carbon nanotubes shows an L_3 peak with much

lower intensity and an L_2 peak at a distance of 13.2 eV, indicating oxidized iron particles.

Raman spectroscopy is widely used to investigate structural changes in carbonaceous materials. The spectra of graphene and G-CNT-Fe synthesized by the ferrocene method are plotted in Figure 4d. The Raman spectrum of carbonaceous material is characterized by three main features. In the case of graphene, a G mode due to the emission of zone-center optical phonons is usually observed at $\sim$1575 cm^{-1}, a disorder induced D mode is seen at $\sim$1350 cm^{-1}, and a symmetry-allowed 2D overtone is detected at $\sim$2700 cm^{-1}. The G band spectra of graphene oxide show a peak at 1582 cm^{-1}, which is attributed to the stretching of the carbon−carbon bond in graphene, whereas this peak in the G-CNT-Fe is shifted to 1583 cm^{-1} associated with bamboo CNTs. In the case of D-band peaks, the D band spectra of graphene oxide and G-CNT-Fe show a peak at 1351 cm^{-1} and 1354 cm^{-1}, respectively. Although the shift at the band
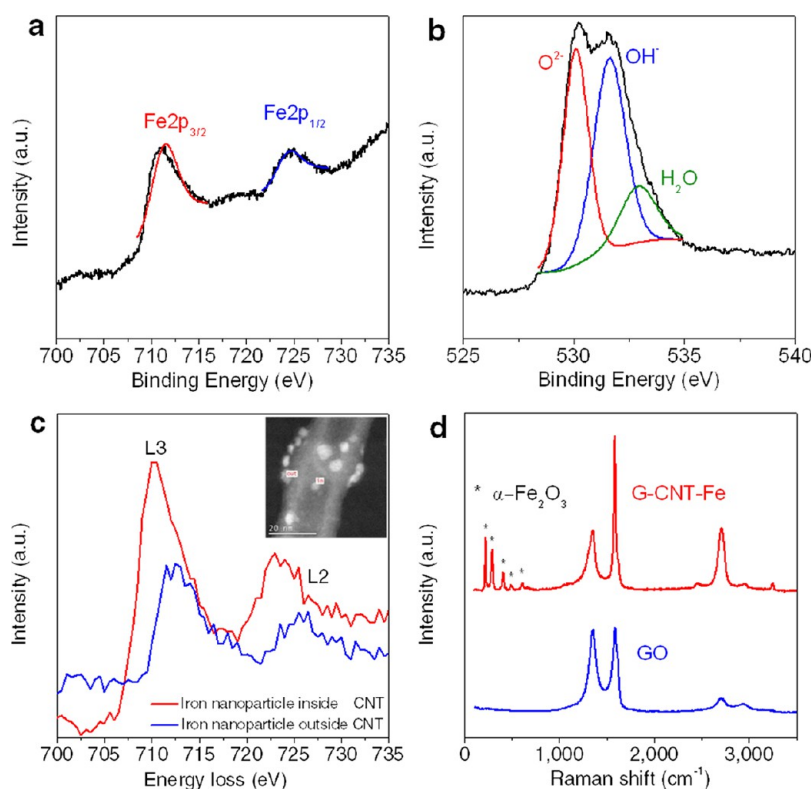
Figure 4. XPS, EELS and Raman Spectra of 3D nanostructure. Deconvoluted Fe2p (a) and O1s (b) XPS spectra of iron, (c) high-resolution EELS spectra of iron nanoparticles inside and outside of the carbon nanotubes, and (d) Raman spectra of graphene oxide and G-CNT-Fe.

locations is not significant, the shapes of the peaks provide valuable information regarding the defects. The G-band of G-CNT-Fe at 1583 cm^{-1} is significantly narrower and thinner than that in graphene. The D-band in graphene oxide at 1351 cm^{-1} and the D′-shoulder at 1620 cm^{-1} have been attributed to the structural disorder at defect sites and finite size effects, respectively. In the case of G-CNT-Fe nanostructure, this D′ band at the 1620 cm^{-1} peak is considerably weaker, indicating 'partial-healing' of defects by the grown carbon nanotubes. More information confirming the growth of CNTs can be obtained from the second-order Raman spectra, the main lines of which are at ~2700 cm^{-1} (2D), 2925 cm^{-1} (D + G), 3150 cm^{-1} (2G), and 3240 cm^{-1} (2D′). After CNT growth, considerable sharpening and increase in the intensity of the peaks was observed. Another interesting observation is the presence of iron-related peaks in the G-CNT-Fe samples, the prominent peaks being located at 224.1, 291.8, and 411.1 cm^{-1}. The most intense of these peaks occurred at 224.1 cm^{-1} and is attributed to maghemite, the alpha phase of Fe_2O_3. Furthermore, the peak at 512.71 cm^{-1} is also attributed to maghemite. The minor peak at 611 cm^{-1} is associated with hematite. The Raman spectra indicate that the main iron particles decorated on the G-CNT-Fe 3D nanostructure are the alpha form of Fe_2O_3, and small portions of different forms are attached with a mixed valence state, further validating the previous XPS and EELS analyses.

Anode Performance in Lithium Ion Battery. Galvanostatic charge−discharge studies were carried out to investigate the applicability of hierarchical G-CNT-Fe nanomaterials as anode electrodes for lithium ion batteries. Figure 5a presents the voltage profiles for charge and discharge of a Li^+/G-CNT-Fe cell recorded at a current density of 100 mAg^{-1} in the potential range of 0 to 3 V. This demonstrates that the discharge curve of the first lithiation process shows significant difference when compared to those of the next cycles. Poizot *et al.* have reported that this difference results from Li-driven, textural or structural modification during the initial discharge process.[33] After the second cycle, the discharge curves are almost overlapping, indicating that the lithium reversibility of the cell was stabilized after subsequent cycling up to 40 cycles, which can be clearly seen in Figure 5b. The discharge curves from the second cycle exhibit two obvious potential plateaus at about ~1.6 and 0.8 V, which are similar to those of Fe_2O_3 reported elsewhere.[34,35] The sloping region between 1.6 and 1 V corresponds to Li-ion insertion into the composite structure and the transformation of Fe^{3+} to Fe^{2+}. A longer discharge plateau appears near 0.85 V and is attributed to the formation of highly irreversible cubic $Li_2Fe_2O_3$ accompanied by a further reduction of this phase to metallic iron *ca.* Fe^{2+} to Fe^0.[36] During the first discharge, a steep decrease in the voltage was observed at ~1.15 V. Thereafter, a plateau
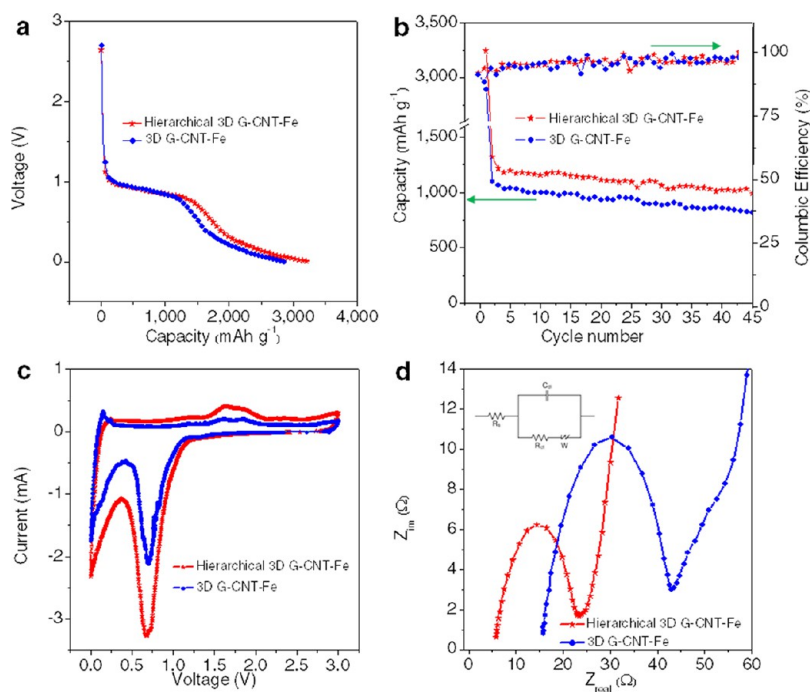
Figure 5. Anode performance of hierarchical 3D graphene–nanotube–iron nanostructure. (a) First discharge curves of a Li^+/G-CNT-Fe cell recorded at 100 mA·g^{-1} current density in the potential range of 0–3 V; (b) specific capacity and Coulombic efficiency of anode electrodes for both baseline and hierarchical 3D G-CNT-Fe nanomaterial; (c) C–V responses of baseline and hierarchical 3D G-CNT-Fe nanomaterial; (d) impedance responses of baseline and hierarchical 3D G-CNT-Fe nanomaterial.

set in and continued until the capacity reached about 1440 mA·h·g^{-1}, which corresponds to the consumption of 8.6 mol of Li/mol of Fe_2O_3. Another discharge plateau at ∼0.85 V, corresponding to a capacity of 1110 mA·h·g^{-1}, was observed followed by a gradual decrease in voltage until 0 V was reached. At the end of the first discharge, the total capacity of 3240 ± 10 mA·h·g^{-1} was achieved. This value corresponds to a consumption of 19.4 mol of Li/mol of Fe_2O_3. In general, it was expected that there would be a maximum uptake of 6 mols of Li per mole of Fe_2O_3 according to the full reduction of Fe^{3+} to Fe^0. The excess capacity delivered by the G-CNT-Fe nanocomposite results from the formation of a solid-electrolyte interface (SEI) layer on the surface of the 3D nanostructure, which is expected to occur in the 0.85 V region.
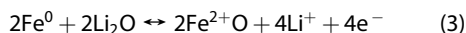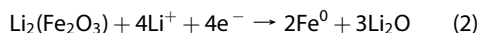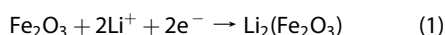
In spite of achieving a maximum capacity of over 3000 mA·h·g^{-1} in the first cycle, electrochemical equilibrium was achieved after the end of the first charge resulting in a stable two-plateau discharge profile as observed from the second discharge onward. This interpretation corroborated well with the single and double peaks observed in the first and second cycles in cyclic voltammetry (CV) testing, respectively. In addition, the reversible capacity loss associated with SEI formation that is usually observed in the first charge–discharge cycle for high surface area anodes was also observed in the present investigation. Similar trends have also been reported for high-performance iron oxide composites, such as carbon/Fe_2O_3, graphene/Fe_2O_3, and SWNT/Fe_2O_3.[36,37] Moreover, the consumption

of 19.4 mol of Li is superior to other values reported elsewhere for iron-based composite electrodes.[38,39] These results clearly reveal that the morphology of the G-CNT-Fe 3D nanostructure plays a crucial role in its electrochemical performance.

Figure 5b shows the cycle performance of a Li^+/G-CNT-Fe cell at 100 mA·g^{-1} in the 0–3 V potential region. It is evident that the difference in discharge capacity between the first and second cycle is quite large due to the formation of the SEI layer which is completed at the end of the first cycle. Note that from the second cycle onward, the capacity appears to stabilize and the Coulombic efficiency was more than 99% after the second cycle. As seen in Figure 5b, the hierarchical G-CNT-Fe 3D nanostructure delivered an initial capacity of 3240 mA·h·g^{-1} and a reversible capacity of 1024 mA·h·g^{-1} even after 40 cycles. The G-CNT-Fe 3D nanostructure provided the first specific capacity of 2892 mA·h·g^{-1}, and the specific capacity achieved after 40 charge/discharge cycles was ∼865 mA·h·g^{-1}. Note that the G-CNT-Fe 3D structure is obtained after the first microwave irradiation and contains only large CNT stems but no CNT branches growing off the stems. The hierarchical G-CNT-Fe 3D structure is obtained after the second microwave irradiation and contains both the CNT stems and branches as shown in Figure 2e. It should be noted that the capacity values reported here are much higher than that of Fe_2O_3 (450 mA·h·g^{-1}) or graphene electrodes (500–700 mA·h·g^{-1}) when tested individually as electrode materials. Such behavior has been

reported previously with other forms of composite electrodes. For example, Yu *et al.* have reported the preparation of a CNT/Fe_2O_3 composite[39] which delivers a capacity of 768 mA·h·g^{-1} after 40 cycles. Zhu *et al.* also reported a reversible capacity of ~980 mA·h·g^{-1} from a graphene/Fe_2O_3 composite after 50 cycles.[37] These studies suggest that there exists a synergy between the CNT, Fe_2O_3 and graphene phases in the composite. In the present study, we have combined all three phases into a single hierarchical architecture, which prevents restacking of the graphene planes due to the CNT spacers, strongly anchors the iron nanoparticles to the graphene and CNT planes, and improves the utilization of the iron particles during the charge—discharge process. The resulting hierarchical, open pore, high surface area electrode structure enables greater number of Li-ions to be inserted and stored within the network resulting in specific capacities of 1024 mA·h·g^{-1} after prolonged cycling along with a Coulombic efficiency in excess of 99% which makes it a promising material for Li-ion battery applications.

To investigate the electrochemical reactions associated with charging and discharging, cyclic voltammetry (CV) was performed on Li$^+$/ G-CNT-Fe cells between 0 and 3 V at a 0.05 mV·s^{-1} scan rate, and the results are presented in Figure 5c. There was one peak observed around 0.8 V during the cathodic process, and the corresponding anode peak appeared at 1.75 V during the discharging process. The first peak indicates the formation of Li_2O species, which results from the conversion reaction of Li$^+$ intercalation. The latter is attributed to the reversible oxidation of Fe^0 to Fe^{3+}. According to the CV studies, the possible mechanism of Li and G-CNT-Fe interaction can be written as[34,35]

$$Fe_2O_3 + 2Li^+ + 2e^- \rightarrow Li_2(Fe_2O_3) \quad (1)$$

$$Li_2(Fe_2O_3) + 4Li^+ + 4e^- \rightarrow 2Fe^0 + 3Li_2O \quad (2)$$

$$2Fe^0 + 2Li_2O \leftrightarrow 2Fe^{2+}O + 4Li^+ + 4e^- \quad (3)$$

During the charging process, the reduction of Fe^{3+} ions to metallic Fe^0 and the formation of amorphous Li_2O occur. The corresponding discharge process is given as expressed in eq 3. It is clear from the above equations that large amount of Li ions can be stored in the Fe_2O_3 structure through the formation and decomposition of Li_2O accompanied by the redox reaction of metallic iron during the anodic process. Additionally, the hierarchical G-CNT-Fe nanostructure shows much larger capacitance than the baseline G-CNT-Fe nanostructure, resulting in better performance as an anode material.

To investigate the effect of graphene and CNT on the conductivity of both baseline and hierarchical G-CNT-Fe nanostructure electrodes, the EIS spectra were recorded from 100 mHz to 100 MHz, and the corresponding Nyquist plots are presented in Figure 5d. Both the spectra were similar in shape, which consisted of a semicircle in the high-frequency region and an inclined line in the low-frequency region. The semicircle in the high-frequency region is attributed to the charge transfer resistance (R_{ct}). The R_{ct} represents the sum of the electrode/electrolyte resistance, that is, the electrode resistance and the resistance associated with the migration of Li$^+$ through the bulk of the electrode. According to the fitted data inserted in Figure 4d, the hierarchical and baseline G-CNT-Fe nanostructure electrodes have R_{ct} values of 5 and 15 Ω, respectively. The values could be considered to be small when compared to the values reported for composites and iron oxide in previous studies.[35,40] Lowering the R_{ct} permits improving the charge transfer characteristics, which in turn enhance the Li$^+$ diffusion rate toward the electrode and increases the electrochemical performance of the materials. Furthermore, the following studies to reduce the gap between initial and reversible capacities should be performed for practical commercialization of the 3D carbon nanostructure through careful and experimental work in near future.

CONCLUSION

In summary, we have developed a fast and facile microwave method to synthesize a novel G-CNT-Fe 3D functional nanostructure composed of stem carbon nanotubes grown on graphene sheets and much smaller branched carbon nanotubes grown again on both the stem nanotubes and on the graphene sheets. In addition, functional 0D iron nanoparticles are embedded in the network creating a unique 3D ensemble of 0D iron nanoparticles distributed on 1D carbon nanotubes and 2D graphene nanosheets. Raman spectra and XPS indicated the presence of iron moieties in mixed valence states of FeOOH and Fe_2O_3, which was further validated by nanoscale EELS data. The obtained hierarchical G-CNT-Fe 3D nanostructure exhibited very high lithium storage capacity significantly above that of its individual constituents indicating a strong synergy between the graphene, CNT, and iron oxide phases in the hierarchical structure.

METHODS

Hierarchical 3D G-CNT-Fe Nanostructure. Expandable graphite oxide was synthesized from natural graphite (Samjung C&G, 99.95%, average size of 200 μm) by a modified Hummers method. Ferrocene (Fe(C_5H_5)$_2$, 98%) and azodicarbonamide ($C_2H_4O_2N_4$, 97%) were purchased from Aldrich and used as received. Expandable graphite oxide platelet was dispersed in acetonitrile, and 0.1 g of ADC and 0.5 g of ferrocene were added

and ultrasonicated for 20 min. This mixture was subjected to microwave irradiation in a microwave reactor (KR-H20MT, Daewoo Electronics Co. Ltd., Korea) at 700 W for 120 s. For constructing a structural hierarchy, subsequent multiple microwave irradiations were performed again each for 30 s after cooling-down and turning off.

Measurements. SEM micrographs were recorded using a Nova NanoSEM 230 FEI at 1 kV in gentle-beam mode without any metal coating. TEM micrographs were recorded on a JEM-3011 HR microscope using a holey-carbon-coated copper grid. EELS spectra were recorded on a JEM-ARM200F microscope operated at 200 kV using a holey-carbon-coated copper grid. For both TEM and EELS studies, a drop of very dilute dispersion after settling was placed on respective substrates and dried under ambient conditions. Raman spectra were recorded on a LabRAM HR UV/vis/NIR (Horiba JobinYvon, France) using a CW Ar-ion laser (514.5 nm) as an excitation source focused through a confocal microscope (BXFM, Olympus, Japan) equipped with an objective lens (50×, numerical aperture = 0.50). High-resolution X-ray photoelectron spectroscopy was carried out with a Multilab 2000 system (VG, U.K.) spectrometer using nonmonochromatic Mg Kα X-ray sources. The XPS spectra were curve-fitted with a mixed Gaussian−Lorentzian shape using the XPS peak analysis software, PEAK.

Anode Performance Test. Electrochemical measurements were performed with a CR2032 coin-type cell in the voltage range of 0−3 V under the current density of 100 mA·g^{-1} using a computer-controlled multichannel battery test unit (WBCS 3000, Won-A-Tech, Korea). The G-CNT-Fe nanohybrid acted as an anode electrode, and lithium foil was used as a cathode. The anode for coin cells was prepared by mixing accurately weighed (G-CNT-Fe, 70 wt %) active material along with ketjen black as conducting additives (KB, 15 wt %), and Teflonized acetylene black (TAB, 15 wt %) as binder. The material was pressed on a 200 mm^2 nickel mesh and subsequently dried at 160 ∘C for 4 h in a vacuum oven. The test cell was fabricated in an argon-filled glovebox by pressing together a lithium foil cathode and nanohybrid anode between a porous polypropylene separator (Celgard 3401) in 1 M LiPF$_6$ in an ethylene carbonate (EC)/dimethyl carbonate (DMC) (1:1 by v/v, Techno Semichem Co., Ltd., Korea) mixture. In the CV measurements, Li metal acted as both the counter and reference electrode in the potential window of 0−3.0 V at a scan rate of 0.05 mV/s using a Solartron electrochemical analyzer (1287, Ameteck, U.K.). Electrochemical impedance spectroscopy (EIS) was performed using a Bio-Logic electrochemical work station (SP-150, Biologic, France) with a three electrode cell configuration.

Conflict of Interest: The authors declare no competing financial interest.

REFERENCES AND NOTES

1. Novoselov, K. S.; Geim, A. K.; Morozov, S. V.; Jiang, D.; Zhang, Y.; Dubonos, S. V.; Grigorieva, I. V.; Firsov, A. A. Electric Field Effect in Atomically Thin Carbon Films. *Science* **2004**, *306*, 666–669.
2. Geim, A. K.; Novoselov, K. S. The Rise of Graphene. *Nat. Mater.* **2007**, *6*, 183–191.
3. Lee, C.; Wei, X. D.; Kysar, J. W.; Hone, J. Measurement of the Elastic Properties and Intrinsic Strength of Monolayer Graphene. *Science* **2008**, *321*, 385–388.
4. Balandin, A. A. Thermal Properties of Graphene and Nanostructured Carbon Materials. *Nat. Mater.* **2011**, *10*, 569–581.
5. Yang, H.; Heo, J.; Park, S.; Song, H. J.; Seo, D. H.; Byun, K. E.; Kim, P.; Yoo, I.; Chung, H. J.; Kim, K. Graphene Barristor, a Triode Device with a Gate-Controlled Schottky Barrier. *Science* **2012**, *336*, 1140–1143.
6. Stoller, M. D.; Park, S. J.; Zhu, Y. W.; An, J. H.; Ruoff, R. S. Graphene-Based Ultracapacitors. *Nano Lett.* **2008**, *8*, 3498–3502.
7. Reddy, A. L. M.; Srivastava, A.; Gowda, S. R.; Gullapalli, H.; Dubey, M.; Ajayan, P. M. Synthesis of Nitrogen-Doped Graphene Films for Lithium Battery Application. *ACS Nano* **2010**, *4*, 6337–6342.
8. Wang, X.; Zhi, L. J.; Mullen, K. Transparent, Conductive Graphene Electrodes for Dye-Sensitized Solar Cells. *Nano Lett.* **2008**, *8*, 323–327.
9. Jung, J. H.; Jeon, J. H.; Sridhar, V.; Oh, I. K. Electro-Active Graphene-Nafion Actuators. *Carbon* **2011**, *49*, 1279–1289.
10. Schedin, F.; Geim, A. K.; Morozov, S. V.; Hill, E. W.; Blake, P.; Katsnelson, M. I.; Novoselov, K. S. Detection of Individual Gas Molecules Adsorbed on Graphene. *Nat. Mater.* **2007**, *6*, 652–655.
11. Terrones, M.; Martin, O.; Gonzalez, M.; Pozuelo, J.; Serrano, B.; Cabanelas, J. C.; Vega-Diaz, S. M.; Baselga, J. Interphases in Graphene Polymer-Based Nanocomposites: Achievements and Challenges. *Adv. Mater.* **2011**, *23*, 5302–5310.
12. Sridhar, V.; Oh, I. K. A Coagulation Technique for Purification of Graphene Sheets with Graphene-Reinforced PVA Hydrogel as Byproduct. *J. Colloid Interface Sci.* **2010**, *348*, 384–387.
13. Guo, Y. L.; Wu, B.; Liu, H. T.; Ma, Y. Q.; Yang, Y.; Zheng, J.; Yu, G.; Liu, Y. Q. Electrical Assembly and Reduction of Graphene Oxide in a Single Solution Step for Use in Flexible Sensors. *Adv. Mater.* **2011**, *23*, 4626–4630.
14. Jafri, R. I.; Rajalakshmi, N.; Ramaprabhu, S. Nitrogen Doped Graphene Nanoplatelets as Catalyst Support for Oxygen Reduction Reaction in Proton Exchange Membrane Fuel Cell. *J. Mater. Chem.* **2010**, *20*, 7114–7117.
15. Luo, B.; Fang, Y.; Wang, B.; Zhou, J. S.; Song, H. H.; Zhi, L. J. Two Dimensional Graphene-SnS$_2$ Hybrids with Superior Rate Capability for Lithium Ion Storage. *Energy Environ. Sci.* **2012**, *5*, 5226–5230.
16. Fei, J. B.; Cui, Y.; Zhao, J.; Gao, L.; Yang, Y.; Li, J. B. Large-Scale Preparation of 3D Self-Assembled Iron Hydroxide and Oxide Hierarchical Nanostructures and Their Applications for Water Treatment. *J. Mater. Chem.* **2011**, *21*, 11742–11746.
17. Jin, J.; Wang, X.; Song, M. Graphene-Based Nanostructured Hybrid Materials for Conductive and Superhydrophobic Functional Coatings. *J. Nanosci. Nanotechnol.* **2011**, *11*, 7715–7722.
18. Kim, U. J.; Lee, I. H.; Bae, J. J.; Lee, S.; Han, G. H.; Chae, S. J.; Gunes, F.; Choi, J. H.; Baik, C. W.; Kim, S. I.; et al. Graphene/Carbon Nanotube Hybrid-Based Transparent 2D Optical Array. *Adv. Mater.* **2011**, *23*, 3809–3810.
19. Hong, T.-K.; Lee, D. W.; Choi, H. J.; Shin, H. S.; Kim, B.-S. Transparent, Flexible Conducting Hybrid Multilayer Thin Films of Multiwalled Carbon Nanotubes with Graphene Nanosheets. *ACS Nano* **2010**, *4*, 3861–3868.
20. Li, S. S.; Luo, Y. H.; Lv, W.; Yu, W. J.; Wu, S. D.; Hou, P. X.; Yang, Q. H.; Meng, Q. B.; Liu, C.; Cheng, H. M. Vertically Aligned Carbon Nanotubes Grown on Graphene Paper as Electrodes in Lithium-Ion Batteries and Dye-Sensitized Solar Cells. *Adv. Energy Mater.* **2011**, *1*, 486–490.
21. Lee, J. M.; Pyun, Y. B.; Yi, J.; Choung, J. W.; Park, W. I. ZnO Nanorod-Graphene Hybrid Architectures for Multifunctional Conductors. *J. Phys. Chem. C* **2009**, *113*, 19134–19138.
22. Sun, Y.; Hu, X.; Luo, W.; Huang, Y. Self-Assembled Hierarchical MoO2/Grpahene Nanoarchitectures and Their Application as a High-Performance Anode Material for Lithium Ion Batteries. *ACS Nano* **2011**, *5*, 7100–7107.
23. Sridhar, V.; Kim, H. J.; Jung, J. H.; Lee, C.; Park, S.; Oh, I. K. Defect-Engineered Three-Dimensional Graphene-Nanotube-Palladium Nanostructures with Ultrahigh Capacitance. *ACS Nano* **2012**, *6*, 10562–10570.
24. Bhushan, B. Biomimetics: Lessons from Nature—An Overview. *Philos. Trans. R. Soc., A* **2009**, *367*, 1445–1486.
25. Espinosa, H. D.; Juster, A. L.; Latourte, F. J.; Loh, O. Y.; Gregoire, D.; Zavattieri, P. D. Tablet-Level Origin of Toughening in Abalone Shells and Translation to Synthetic Composite Materials. *Nat. Commun.* **2011**, *2*, 173.

26. Muller, R. Hierarchical Microimaging of Bone Structure and Function. *Nat. Rev. Rheumatol.* **2009**, *5*, 373–381.

27. Zhang, Z. Q.; Zhang, Y. W.; Gao, H. J. On Optimal Hierarchy of Load-Bearing Biological Materials. *Proc. R. Soc. B* **2011**, *278*, 519–525.

28. Yao, H.; Gao, H. Mechanics of Robust and Releasable Adhesion in Biology: Bottom-Up Designed Hierarchical Structures of Gecko. *J. Mech. Phys. Solids* **2006**, *54*, 1120–1146.

29. Chaudhary, S.; Lu, H. W.; Muller, A. M.; Bardeen, C. J.; Ozkan, M. Hierarchical Placement and Associated Optoelectronic Impact of Carbon Nanotubes in Polymer-Fullerene Solar Cells. *Nano Lett.* **2007**, *7*, 1973–1979.

30. Tan, J. P. K.; Kim, S. H.; Nederberg, F.; Appel, E. A.; Waymouth, R. M.; Zhang, Y.; Hedrick, J. L.; Yang, Y. Y. Hierarchical Supermolecular Structures for Sustained Drug Release. *Small* **2009**, *5*, 1504–1507.

31. Yin, S.; Zhang, Y.; Kong, J.; Zou, C.; Li, C. M.; Lu, X.; Ma, J.; Boey, F. Y. C.; Chen, X. Assembly of Graphene Sheets into Hierarchical Structures for High-Performance Energy Storage. *ACS Nano* **2011**, *5*, 3831–3838.

32. Lin, M.; Tan, J. P. Y.; Boothroyd, C.; Loh, K. P.; Tok, E. S.; Foo, Y. L. Dynamical Abservation of Bamboo-like Carbon Nanotube Growth. *Nano Lett.* **2007**, *7*, 2234–2238.

33. Poizot, P.; Laruelle, S.; Grugeon, S.; Dupont, L.; Tarascon, J. M. Nano-Sized Transition-Metal Oxides as Negative-Electrode Materials for Lithium-Ion Batteries. *Nature* **2000**, *407*, 496–499.

34. Chen, J.; Xu, L. N.; Li, W. Y.; Gou, X. L. α-Fe$_2$O$_3$ Nanotubes in Gas Aensor and Lithium-Ion Battery Applications. *Adv. Mater.* **2005**, *17*, 582–586.

35. Reddy, M. V.; Yu, T.; Sow, C. H.; Shen, Z. X.; Lim, C. T.; Rao, G. V. S.; Chowdari, B. V. R. α-Fe$_2$O$_3$ Nanoflakes as an Anode Material for Li-Aon batteries. *Adv. Funct. Mater.* **2007**, *17*, 2792–2799.

36. Larcher, D.; Masquelier, C.; Bonnin, D.; Chabre, Y.; Masson, V.; Leriche, J. B.; Tarascon, J. M. Effect of Particle Size on Aithium Intercalation into α-Fe$_2$O$_3$. *J. Electrochem. Soc.* **2003**, *150*, A133–A139.

37. Zhu, X. J.; Zhu, Y. W.; Murali, S.; Stollers, M. D.; Ruoff, R. S. Nanostructured Reduced Graphene Oxide/Fe$_2$O$_3$ Composite as a High-Performance Anode Material for Lithium Ion Batteries. *ACS Nano* **2011**, *5*, 3333–3338.

38. Morales, J.; Sanchez, L.; Martin, F.; Berry, F.; Ren, X. L. Synthesis and Characterization of Nanometric Iron and Iron-Titanium Oxides by Mechanical Milling: Electrochemical Properties as Anodic Materials in Lithium Cells. *J. Electrochem. Soc.* **2005**, *152*, A1748–A1754.

39. Yu, W. J.; Hou, P. X.; Zhang, L. L.; Li, F.; Liu, C.; Cheng, H. M. Preparation and Electrochemical Property of Fe$_2$O$_3$ nanoparticles-Filled Carbon Aanotubes. *Chem. Commun.* **2010**, *46*, 8576–8578.

40. Wang, G.; Liu, T.; Luo, Y. J.; Zhao, Y.; Ren, Z. Y.; Bai, J. B.; Wang, H. Preparation of Fe$_2$O$_3$/Graphene Composite and Its Electrochemical Performance as an Anode Material for Lithium Ion Batteries. *J. Alloys Compd.* **2011**, *509*, L216–L220.